

CHAPTER e29

Atlas of Noninvasive Cardiac Imaging

Rick A Nishimura

Panithya Chareonthitawee

Matthew Martinez

ECHOCARDIOGRAPHIC IMAGES

Video e29-1 Real-time two-dimensional echocardiographic images of a patient with a normal heart. **A. (Play video)** Parasternal long-axis view. **B. (Play video)** Parasternal short-axis view. There is symmetric contraction of the ventricles, evidenced by a decrease in cavity size and increase in wall thickness during systole. Echocardiographic imaging is performed in multiple acoustic windows with different transducer rotations so that the entire heart and great vessels can be displayed in various planes. Most information from a study is obtained from visual analysis of the two-dimensional images, although objective measurements of cardiac dimensions can be made.

Video e29-2 Real-time two-dimensional echocardiographic images of a patient with a severe decrease in left ventricular systolic function. The estimated ejection fraction is 20%. **A. (Play video)** Parasternal long-axis view. **B. (Play video)** Parasternal short-axis view.

Video e29-3 Real-time two-dimensional echocardiographic images of a patient with hypertrophic cardiomyopathy. There is a marked increase in left ventricular wall thickness with hyperdynamic systolic function. **A. (Play video)** Parasternal long-axis view. **B. (Play video)** Parasternal short-axis view.

Video e29-4 (Play video) Real-time two-dimensional parasternal long-axis images from a patient with aortic stenosis. There is normal left ventricular cavity size with normal systolic function. The aortic valve is thickened and calcified, with restricted opening.

Video e29-5 Real-time two-dimensional echocardiographic images of a patient with mitral stenosis. There is diastolic doming and restricted leaflet opening secondary to fusion of the commissures. **A. (Play video)** Parasternal long-axis view. **B. (Play video)** Parasternal short-axis view.

Video e29-6 Real-time two-dimensional echocardiographic images from the parasternal long-axis view of a patient with mitral valve prolapse. During systole, both anterior and posterior leaflet of the mitral valve prolapse into the left atrium. **A. (Play video)** Gray-scale images demonstrate a leaflet morphology and motion. **B. (Play video)** Color flow imaging demonstrating late systolic blue-colored jet of mitral regurgitation. Abnormalities of the valve apparatus such as annular dilatation, prolapse, flail leaflets, vegetation, and rheumatic involvement can be diagnosed by two-dimensional echocardiography. The left ventricular response to volume overload can be assessed by two-dimensional echocardiography.

Video e29-7 Real-time two-dimensional images with color flow Doppler imaging of a patient with mitral regurgitation due to ruptured chordae tendineae. **A. (Play video)** Gray-scale image showing a thickened redundant posterior leaflet of the mitral valve with loss of coaptation during systole. **B. (Play video)** Color flow imaging showing severe mitral regurgitation as high velocity turbulence (mosaic pattern) extending into the left atrium during systole.

Video e29-8 (Play video) Real-time transesophageal echocardiographic images of a patient with severe mitral regurgitation due to a flail posterior leaflet. The posterior mitral valve leaflet is completely unsupported and moves into the left atrium during systole. Transesophageal echocardiography provides high-resolution images of posterior structure such as the left atrium, mitral valve, and aorta.

Video e29-9 (Play video) Real-time two-dimensional echocardiographic images of a patient with a vegetation on the mitral valve. There is a mobile echo density attached directly to the mitral valve apparatus that intermittently appears in the left atrium.

Video e29-10 (Play video) Real-time transesophageal echocardiographic images of a patient with a left atrial myxoma. There is a large echo-dense mass in the left atrium that is attached to the atrial septum. The mass moves across the mitral valve during diastole. Although an echocardiographic image cannot provide pathologic confirmation of the etiology of a mass, the diagnosis of atrial myxoma can be suspected from the appearance, mobility, and attachment to the atrial septum.

Video e29-11 (Play video) Real-time two-dimensional echocardiographic images from the parasternal long-axis view of a patient with a large aneurysm of the ascending aorta.

Video e29-12 (Play video) Real-time two-dimensional echocardiographic images of a patient with pericardial effusion. The effusion is shown as a black echo-free space surrounding the heart.

Video e29-13 (Play video) Real-time two-dimensional echocardiographic images from a subcostal view showing a large secundum atrial septal defect. There is a “drop out” in the region of the mid atrial septum. The right ventricle is enlarged from right ventricular volume overload.

Video e29-14 Real-time two-dimensional echocardiographic images showing a close-up view of the atrial septum in a patient with the question of an atrial septal defect. **A. (Play video)** Gray-scale image showing a questionable “drop out” in the atrial septum. **B. (Play video)** Color flow imaging confirms left to right flow across the atrial septum.

Video e29-15 Real-time two-dimensional stress echocardiogram in a normal subject. The studies at rest are shown on the left and the studies during peak exercise are shown on the right. **A. (Play video)** Parasternal long-axis (*top*) and short-axis (*bottom*) views. **B. (Play video)** Apical four-chamber (*top*) and two-chamber (*bottom*) views. At rest, there is contraction of all segments of the myocardium. During exercise, there is an increase in contractility and in the thickening of all segments of the myocardium with a decrease in end-systolic volume.

Video e29-16 Real-time two-dimensional stress echocardiogram of a patient with coronary artery disease. The studies at rest are shown on the left and studies during peak exercise are shown on the right. **A. (Play video)** Parasternal long-axis (*top*) and short-axis (*bottom*) views. **B. (Play video)** Apical four-chamber (*top*) and two-chamber (*bottom*) views. The images during peak exercise show regional wall motion abnormalities in the anteroapical distribution indicative of myocardial ischemia. This was subsequently found to be associated with a high-grade lesion on the left anterior descending artery.

NUCLEAR IMAGES

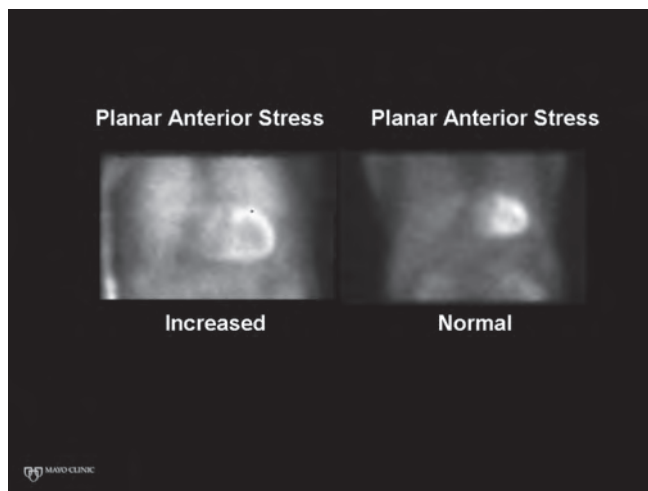


Figure e29-1 Anterior planar thallium images following stress, showing increased lung uptake on the left (count intensity in lung >50% of that in myocardium) and normal lung uptake on the right (count intensity in lung <50% of that in myocardium).

Increased lung uptake of thallium may be seen immediately after stress. It reflects increased pulmonary capillary wedge pressure and occurs in the presence of severe coronary artery disease and/or left ventricular systolic dysfunction. It provides important adverse prognostic information that is incremental to other clinical, stress, and coronary angiographic variables.

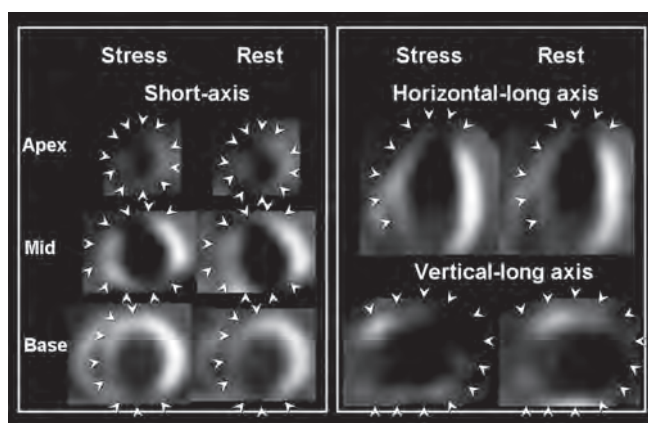


Figure e29-2 Exercise SPECT ^{99m}Tc sestamibi scan in a 64-year-old male patient with a previous infarct. The stress images (left) show a large defect involving the apex, anterior, septal, and inferior walls (arrowheads) with little change from the rest images (right), signifying a fixed defect consistent with infarction. There is also severe left ventricular enlargement and severely reduced left ventricular systolic function by gated images (next image). The relative advantage of ^{201}Tl and ^{99m}Tc are detailed in Table e20-1a. The better image quality and assessment of ventricular function permitted by ^{99m}Tc compounds have contributed to their more common use for stress imaging, although both ^{201}Tl - and ^{99m}Tc -labeled compounds provide clinically useful myocardial perfusion images in the majority of patients. A “dual-isotope” protocol is employed in some centers. This uses ^{201}Tl for the initial rest image and a ^{99m}Tc -labeled compound for the subsequent stress image, primarily for patient and scheduling convenience. SPECT, single photon emission computed tomography; ^{99m}Tc , technetium 99m.

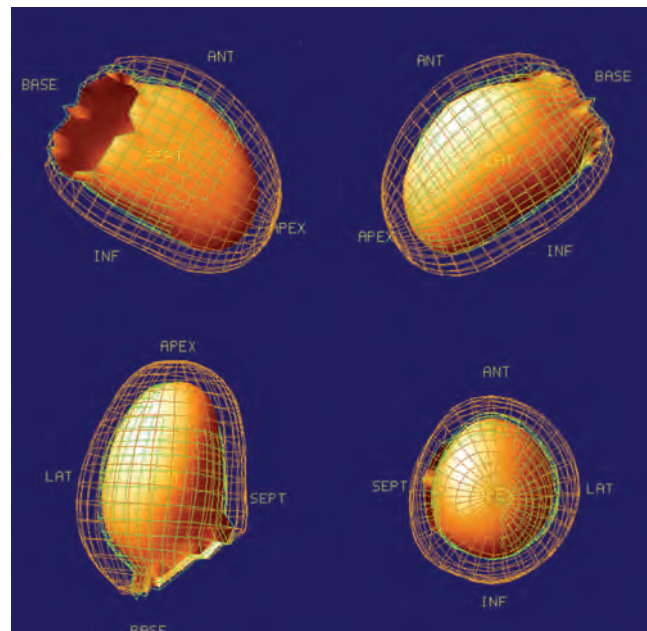


Figure e29-3 Mesh cinegraphic display of images obtained from electrocardiographic gating of a SPECT ^{99m}Tc sestamibi scan in a 64-year-old male patient with a previous infarct (same patient as in Fig. e29-2). Gated images are generally acquired about 30–45 min following stress. Electrocardiographic gating allows calculation of left ventricular volumes and global systolic function, as well as visual assessment of regional wall motion. In this patient, the calculated left ventricular ejection fraction was 13%. There was severe global hypokinesis.

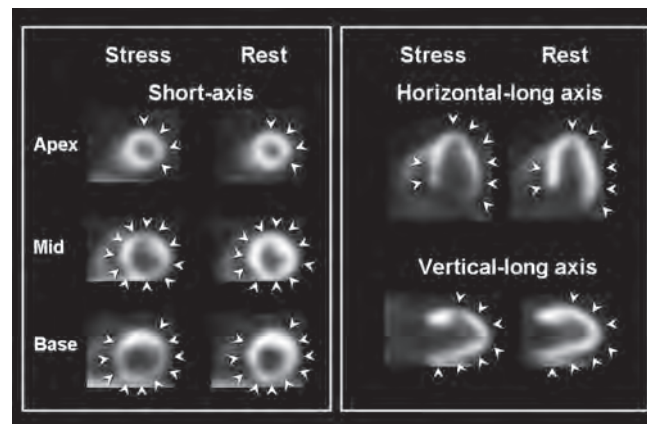


Figure e29-4 Adenosine PET N-13 ammonia in a 55-year-old obese male patient with typical angina. The stress images (left) show a large defect involving the apex, anterior, septal, inferior, and lateral walls (arrowhead) with normal or near-normal tracer uptake in the corresponding regions on the rest images (arrowheads), signifying a reversible defect consistent with ischemia. The patient was found to have severe multivessel coronary artery disease on subsequent invasive angiography.

The robust methods for attenuation correction with PET improve the specificity, particularly in obese populations and women, while the superior resolution and higher extraction fraction of PET tracers increase the sensitivity of detection of coronary artery disease. The excellent image quality of PET has contributed to their emerging use for stress imaging. Additional advantages include assessment of left ventricular volumes and systolic function, shorter imaging protocols, and lower radiation exposure, particularly with N-13 ammonia.

PET, positron emission tomography. SPECT, single photon emission computed tomography.

MRI/CT IMAGES

Video e29-17 (Play video) MRI scan in real time of a patient with a large left ventricular apical aneurysm. The long axis-view demonstrates a thin dyskinetic apical aneurysm with a preserved systolic function of the basal anterior and basal inferior wall. MRI scanning allows excellent visualization of endocardial border.



Figure e29-5 MR image of a patient with a right ventricular myxoma, which is shown as a bright oblong structure in the right ventricular outflow tract.

Video e29-18 (Play video) Cine MRI scan of a patient with a dilated ascending aorta (annulo-aortic ectasia). There is a central jet of aortic regurgitation entering the left ventricular outflow tract.

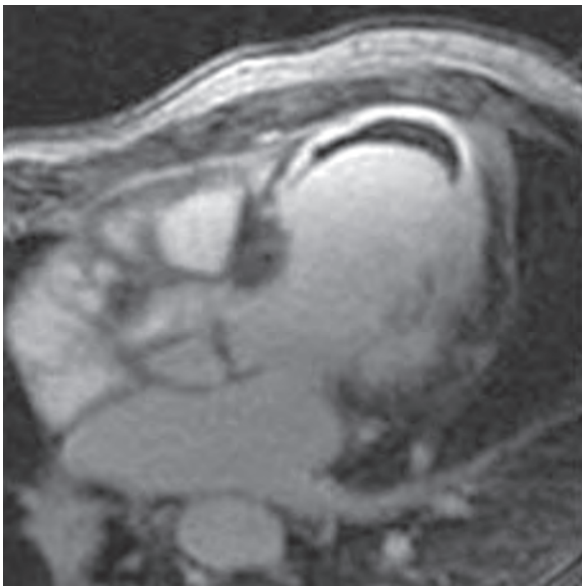


Figure e29-6 MR image with contrast enhancement of a patient with a large apical aneurysm and thrombus. Imaging the heart 10–20 min after gadolinium injection demonstrates enhancement of the infarcted tissue (visible as dense white image). The infarcted tissue retains contrast by virtue of its large extracellular volume. The left ventricular thrombus adherent to the infarcted myocardium is shown as a dark laminated area adjacent to the white myocardium.



Figure e29-7 MR images with contrast enhancement in a patient with acute pericarditis. In the presence of pericardial inflammation, the gadolinium enhancement occurs, seen as a white layer in the pericardium.

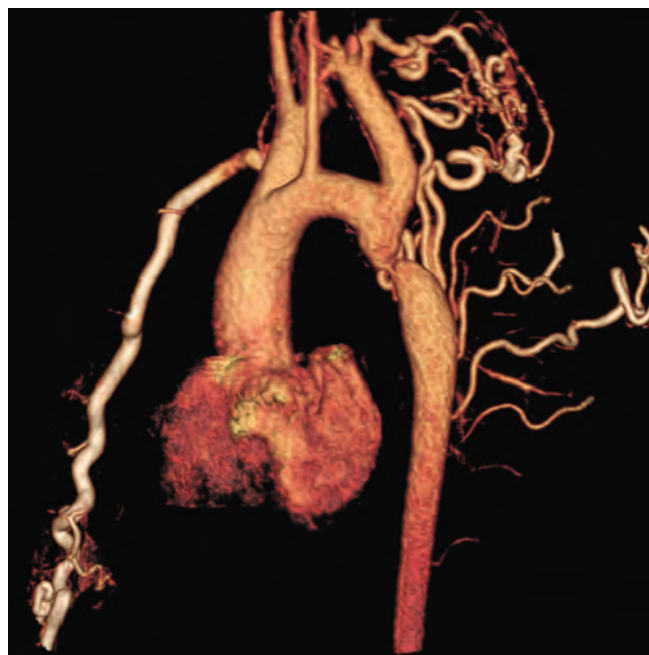


Figure e29-8 Three-dimensional reconstruction of a CT angiogram, showing a severe coarctation of the descending aorta. The large collateral vessels are the result of the severe stenosis of the distal thoracic aorta.

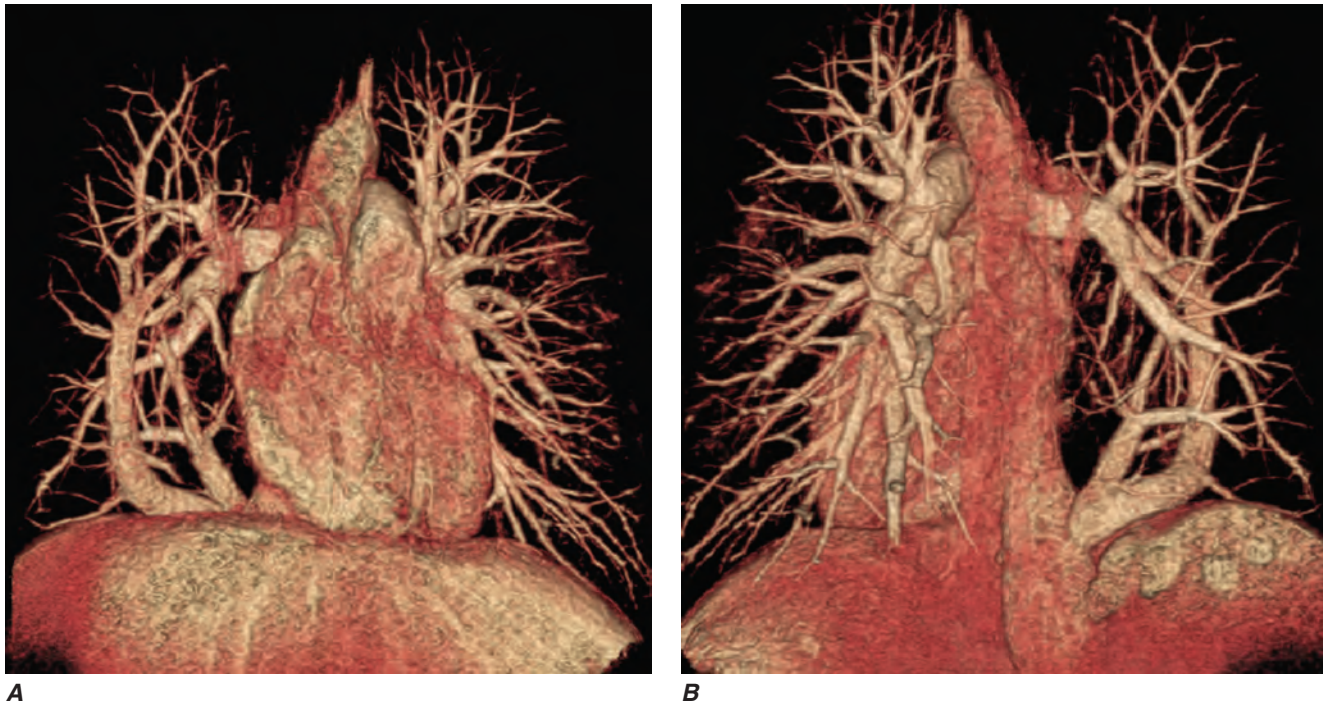


Figure e29-9 Three-dimensional reconstruction of a CT angiogram of the pulmonary veins, demonstrating an anomalous pulmonary venous drainage into the inferior vena cava. **A.**: frontal view. **B.**: posterior view.

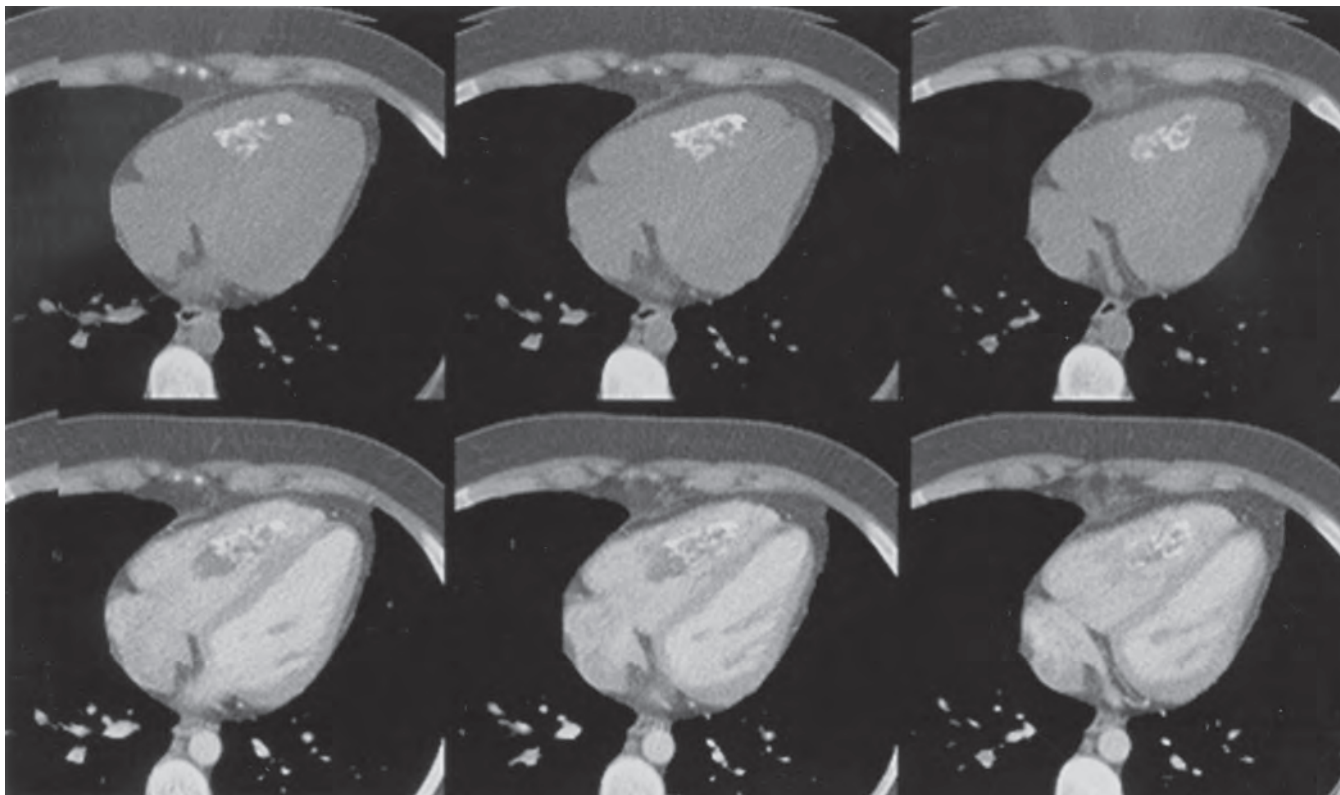


Figure e29-10 Cardiac CT images demonstrating a calcified mass in the right ventricle, which at pathologic examination was a chronic thrombus. Calcification is seen as a bright signal in both the noncontrast (*upper*) and contrast-enhanced (*lower*) images.

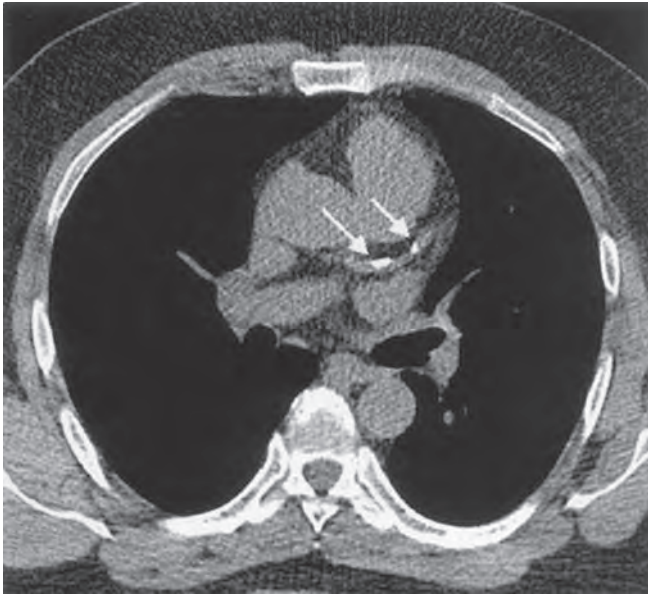


Figure e29-11 Noncontrast image from an electron beam CT revealing two small foci of calcification in the left anterior descending artery (*arrows*).



Figure e29-12 CT image from a patient with calcific constrictive pericarditis. Calcification is seen as a bright signal in the anterior pericardium as well as calcification extending into the lateral wall of the left ventricle.

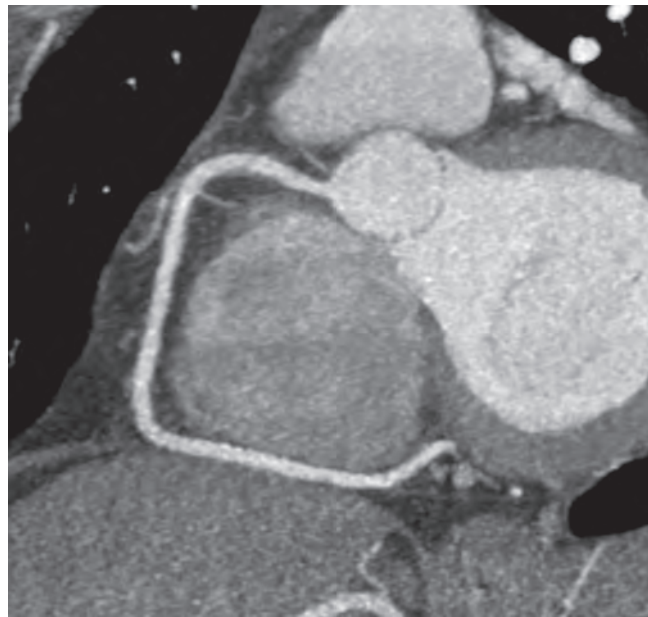


Figure e29-13 A reconstructed CT coronary angiogram showing a normal right coronary artery.

Video e29-19 (Play video) CT coronary angiogram showing a normal right coronary artery. The movie highlights multiple thin slices through the right coronary artery.

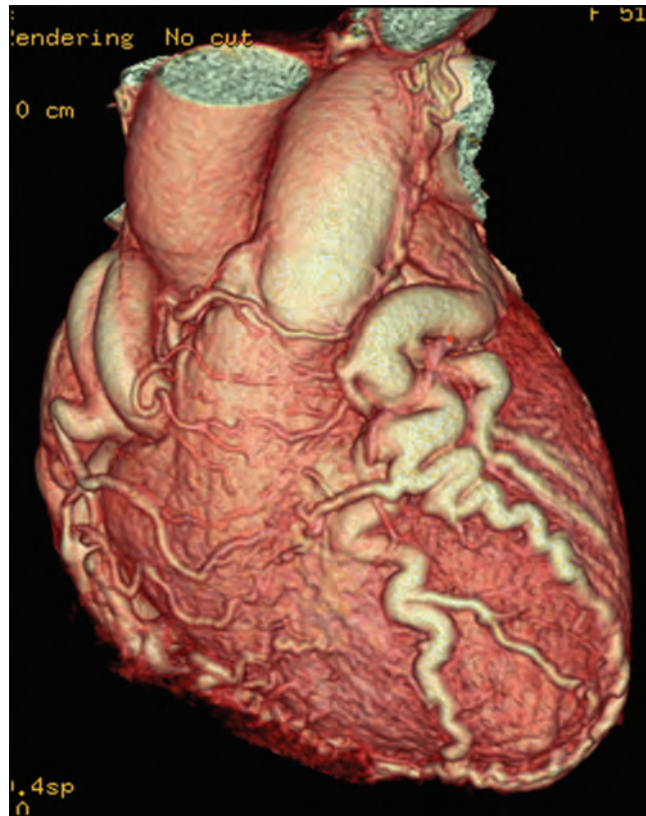


Figure e29-14 Three-dimensional reconstruction of a CT angiogram showing a large fistula of the left anterior descending artery.

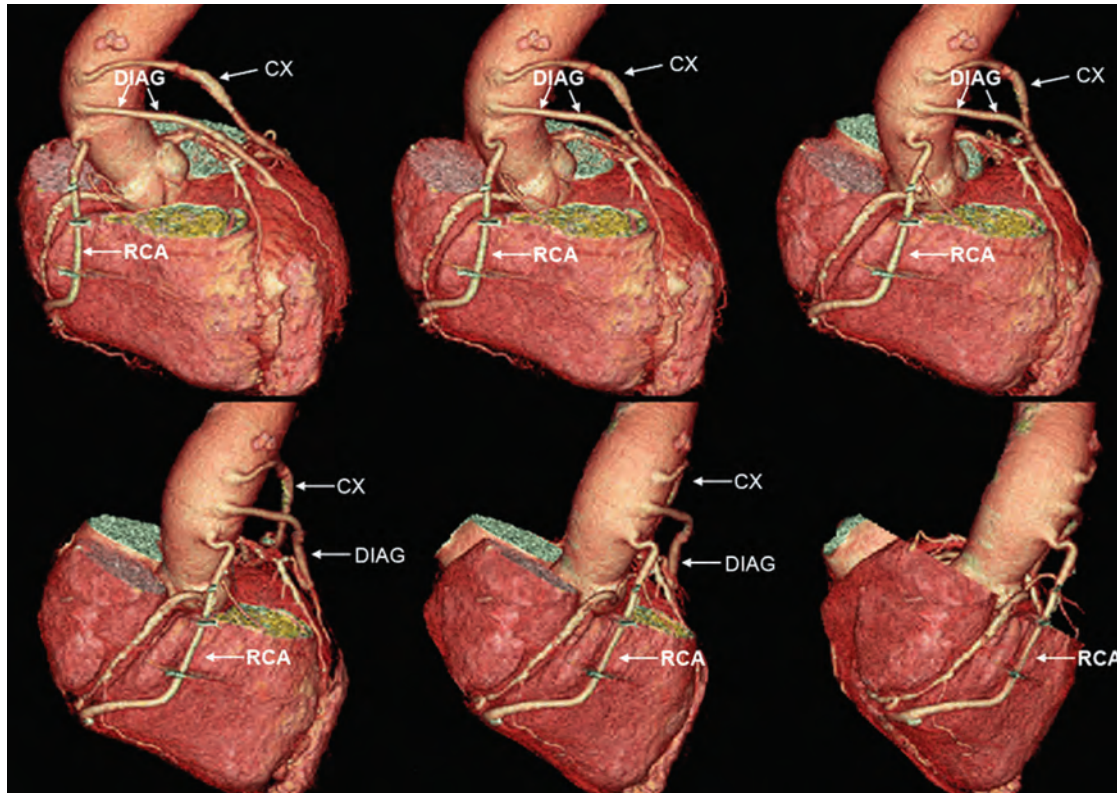


Figure e29-15 Three-dimensional reconstruction of a CT angiogram demonstrating three saphenous vein coronary artery bypass grafts in different views. In the upper left-hand panel is an anterior posterior view of the heart and grafts. The heart is sequentially rotated clockwise in the panels

going from left to right to illustrate the ability of CT angiography to visualize the saphenous vein grafts. RCA: saphenous vein graft to the right coronary artery; CX: saphenous vein graft to the circumflex artery; DIAG: saphenous vein graft to the diagonal artery.